

MIXING IN ZERO AND SOLAR METALLICITY SUPERNOVAE

C.C. JOGGERST^{1,2}, S. E. WOOSLEY¹, & ALEXANDER HEGER^{2,3}

ACCEPTED TO APJ: *October 13, 2008*

ABSTRACT

Two-dimensional simulations of mixing and fall back in non-rotating massive stars have been carried out using realistic initial models for the presupernova star and assuming standard spherically symmetric explosions of 1.2×10^{51} erg. Stars of 15 and 25 M_{\odot} with both primordial and solar composition were modeled. The zero metallicity supernova progenitors were compact blue stars and the amount of Rayleigh-Taylor induced mixing in them was greatly reduced compared with what was seen in the red supergiants with solar metallicity. The compact zero-metal stars also experienced more fallback than their solar metallicity counterparts. As a result, the ejected nucleosynthesis from the two populations was very different. For the simple explosion model assumed, low metallicity stars ejected too little iron and intermediate mass elements even to explain the abundance patterns in the most iron-poor stars found to date, suggesting that some important ingredient is missing. Rotation is likely to alter these conclusions by producing a greater fraction of red supergiants among Population III stars. The velocities of the heavy elements in all models considered - both red and blue supergiants - were less than observed in SN 1987A, suggesting that at least occasionally, asymmetric aspects of the explosion mechanism and fallback play a major role in mixing.

Subject headings: Supernovae, nucleosynthesis, first stars

1. INTRODUCTION

The nucleosynthetic yields of supernovae are important components of galactic chemical evolution and are essential to understanding the abundances observed in metal-poor stars. The yield of a core-collapse supernova is determined by its presupernova evolution, the geometry and energy of its explosion, and by the mixing and fallback that occur as the supernova shock traverses the star (e.g., Chevalier 2005). Mixing and fallback also affect the supernova's light curve and spectrum and the appearance of its remnant. The dense knots and filaments visible in Hubble (Blair et al. 2000) and Chandra (Hughes et al. 2000) images of supernova remnants provide clear evidence that mixing of some sort is a common occurrence. Supernova 1987A, the closest and most thoroughly observed modern supernova, provided important observational constraints on models. Its smooth bolometric light curve required extensive mixing of the helium core with the hydrogen envelope (e.g., Woosley 1988). The early appearance of X-rays and γ -rays from radioactive decay of ^{56}Ni , as well as spectroscopic evidence some fraction of the iron peak was mixed out to 4000 km s^{-1} , provided further evidence for extensive mixing in the interior of the supernova at early times (Arnett et al. 1989; Witteborn et al. 1989; Utrobin 2004).

Differences in the presupernova structure of zero and solar metallicity stars alter the way mixing and fallback processes operate. Below about 40 M_{\odot} , non-rotating, zero-metallicity stars are expected to be more compact than solar-metallicity progenitors (Heger & Woosley 2008; Hirschi et al. 2008). Metal-free gas has a lower

opacity than solar-metallicity gas and lacks initial seed nuclei for the CNO cycle, leading to inefficient hydrogen burning and a very dense hydrogen shell of low entropy in the presupernova stars. Chevalier (1989) predicted that higher amounts of fallback are expected for more compact progenitors. In a recent paper, Zhang et al. (2008) used their one-dimensional Eulerian code PANGU to determine the remnant masses left behind by the supernova models calculated in surveys by Woosley & Heger (2007) and Heger & Woosley (2008). They found that zero-metallicity supernovae experienced more fallback and left behind larger compact remnants than their solar metallicity counterparts. For example, the baryonic remnant masses left behind by 25 M_{\odot} stars of zero and solar metallicity were 4.16 and 2.09 M_{\odot} , respectively.

Different presupernova structures, arising from differences in stellar mass and metallicity, determine where Rayleigh-Taylor instabilities occur and the extent to which they grow. An initially static, incompressible fluid is unstable if the pressure gradient points opposite to the density gradient, i.e., when $(dP/dr)(d\rho/dr) < 0$ (e.g. Chevalier 1976; Benz & Thielemann 1990). The location of these density inversions varies with time as the forward and reverse shocks propagate through the star. Particularly important are regions where the forward shock encounters an increasing value for ρr^3 , where ρ is the density and r , the radius (Herant & Woosley 1994). The time scale also depends upon the initial stellar structure. In particular, a more compact star will experience faster shock propagation, leaving less time for instabilities to grow.

Because SN 1987A was so well observed, most previous studies of Rayleigh-Taylor mixing in core collapse supernovae (Arnett et al. 1989; Fryxell et al. 1991; Mueller et al. 1991; Hachisu et al. 1990, 1992; Herant & Benz 1991, 1992; Kifonidis et al. 2006) have been in the context of that event. Others have studied red supergiant

¹ Department of Astronomy and Astrophysics, University of California at Santa Cruz, Santa Cruz, CA 95060; cchurch@ucolick.org

² Theoretical Astrophysics (T-6), Los Alamos National Laboratory, Los Alamos, NM 87545

³ School of Physics and Astronomy, University of Minnesota, Minneapolis, MN 55455

progenitors (Herant & Woosley 1994). Except for Herant and Woosley, these studies all used red and blue supergiants of 15 to 20 M_{\odot} as progenitors. The methodology of all these studies was similar. A one-dimensional progenitor model was exploded, somewhat artificially, by means of a piston or a thermal bomb, and the subsequent evolution followed with a two-dimensional code.

More recently, Kifonidis et al. (2003) and Kifonidis et al. (2006) have used a different approach. These authors followed a blue supergiant model from the first seconds of the explosion out to about 5 days after core collapse, using first one code with neutrino physics for the early times, and another code with mesh refinement for later times. They saw mixing at the Si-O interface, a location at which no previous studies had found mixing, and were able to reproduce the high ^{56}Ni velocities observed in SN 1987A, something previous studies had not done.

While attempts to reproduce observations of 1987A have been numerous, no multidimensional studies of mixing and fallback in very low metallicity supernovae have been done. The nucleosynthetic yields of metal-free (Pop III) and extremely metal-poor (EMP) stars might still be visible in the abundance patterns observed in some halo stars in our own galaxy. Of particular interest are the “ultra-iron-poor” (HMP) stars (Frebel et al. 2005; Aoki et al. 2006). These stars with $[\text{Fe}/\text{H}] < -5$, have abundance patterns that differ considerably from those observed in stars with near solar metallicity or even other metal-poor stars (Cayrel et al. 2004). It is possible that these iron-poor stars were enriched by only one or a few supernovae (Frebel et al. 2005). In particular, the two most metal-poor stars known and several other UMP stars display marked enhancement in C, N, and O relative to Fe. Previous studies (Iwamoto et al. 2005; Tomimaga et al. 2007; Heger & Woosley 2008) have sought to explain these abundance patterns with one-dimensional models for supernovae that parametrize the amount of mixing and fallback to match what is observed. Simulating mixing and fallback directly, rather than parametrizing, requires a multi-dimensional approach.

In this paper, we use two-dimensional axisymmetric simulations to explore directly the amount of Rayleigh-Taylor-induced mixing that occurs in non-rotating zero- and solar-metallicity stars. Our methodology is similar to the earlier studies (before Kifonidis) of SN 1987A. In § 2, we discuss our initial models, our modifications to the FLASH code, and our simulation setup. In § 3, results are given that show the degree of mixing, the final velocity distribution of isotopes, and the ejected yields. These yields are compared with abundances observed in HMP stars in § 3.4. Finally, we provide a short summary of results and their interpretation in § 4

2. MODELS AND METHODS

The present work follows the method used in many previous studies of mixing in supernovae. A one-dimensional code was used to evolve and explode the pre-supernova model and to follow the first stages of the expansion to the time when the reverse shock was just beginning to form. No significant growth of instabilities is expected before the formation of the reverse shock. The one-dimensional model was then mapped onto a two-dimensional grid and the ensuing instabilities followed.

While Kifonidis et al. (2006) reproduced the observations of SN 1987A somewhat better than previous attempts, possibly by following the early stages of the explosion, this paper does not do that. The physics of the initial explosion remains uncertain and our goal is to isolate the differences in post-explosive mixing that arise as a direct consequence of the differences in initial structure of the pre-supernova models. Exploding the star with a piston in the same location and with the same energy in all models allows us to accomplish this.

The choice of piston mass location is constrained by observational parameters. The piston cannot be located within the iron core or the resulting explosion will produce far too much of $^{54,58}\text{Fe}$ and other neutron-rich species to be in agreement with observations of these isotopes. On the other hand, the remnant mass will be too large to agree with observations if the explosion site is located outside the base of the oxygen shell. There are reasons to believe the location site is located at the base of the oxygen shell—the large density decrease associated with this location is dynamically important, and successful explosion calculations often find the mass cut there.

The papers from which our models are taken also reported on models in which the stars were exploded with a piston at the edge of the Ni core. These explosions experience slightly less fallback, and produce more nickel, by a factor of 2 or so, than the models presented in this paper.

2.1. Progenitor Models

Initial models were taken from the surveys of Heger & Woosley (2008) and Woosley & Heger (2007). Both of these papers used the KEPLER code (Weaver et al. 1978; Woosley et al. 2002) to evolve stars through all stable stages of nuclear burning until their iron cores became unstable to collapse. At this point, pistons located at or near the base of the oxygen shell were used to explode the stars. Heger & Woosley (2008) simulated the evolution and explosion of 10 to 100 M_{\odot} stars with zero initial metallicity. Explosion energies ranged from 0.3 to 10 B, where 1 Bethe = 1 B = 10^{51} ergs. Woosley & Heger (2007) examined solar-metallicity stars from 12 to 100 M_{\odot} which were exploded by pistons similar to the other survey, but for a more limited set of masses and energies. Both surveys were limited to non-rotating progenitors. The zero-metallicity stars were assumed to have no mass loss, while the solar-metallicity models took mass loss into account.

Here only two representative stars from each survey are studied: Models z15D and z25D from Heger & Woosley (2008) and Models s15A and s25A from Woosley & Heger (2007). The letter “z” indicates zero initial metallicity, while “s” indicates solar metallicity. The numbers in the models correspond to the initial mass of the star in M_{\odot} and the final letter is the explosion energy, 1.2 B in each case. The piston was located at the place in the star where the entropy was equal to $4.0k_B/\text{baryon}$. This corresponded to the base of the oxygen shell. Series sA and zD are thus directly comparable in all respects save their initial metallicity. 15 and 25 M_{\odot} represent the “canonical” supernova cases with the most commonly employed explosion energy and piston location. 15 and 25 M_{\odot} stars are also in the same mass range as previous stud-

ies of Rayleigh-Taylor mixing in supernovae, allowing for easy comparison.

The one-dimensional progenitor models used in this study lead to spherically symmetric explosions. Mapping the models from one to two dimensions after the explosion has taken place has the effect of suppressing low-order departures from spherical symmetry. This work only addresses spherically symmetric explosions with asymmetries of significantly higher mode than $l = 1$ or 2.

2.2. The FLASH code

The FLASH code (Fryxell et al. 2000) was used to follow shock propagation and mixing in the models in two dimensions. This code has been extensively verified and tested (Calder et al. 2002; Weirs et al. 2005). FLASH is an adaptive mesh refinement code based on an Eulerian implementation of the Piecewise Parabolic Method (PPM) of Colella & Woodward (1984). The code can be configured in a number of different ways. We used the HLLC Riemann solver to resolve shocks. KEPLER uses 19 different isotopes to evolve stellar models through stable stages of nuclear burning. We use the ‘‘aprox19’’ composition module included with the FLASH2.5 distribution to map these isotopes directly to FLASH. The abundances of 19 different isotopes, from ^1H to ^{56}Ni , are stored for each grid cell. Explosive nuclear burning could have been followed in FLASH using this network, but the burning was over by the time the models were mapped into FLASH. Mapping the star in at earlier times to follow the explosive burning in two dimensions would have had little effect, as no departure from spherical symmetry is expected until the formation of the reverse shock, which occurs much later in the calculation. FLASH was configured to use axisymmetric coordinates. The gravitational potential was computed using a multipole method to solve Poisson’s equation. The mass distribution in this simulation had only slight deviations from spherical symmetry, so the additional gravitational force from overdensities in the simulations was small. The gravitational potential from the point mass at the origin of the grid was added to the potential computed by the multipole solver at each time step. The hydrodynamic equations were solved using an explicit, dimensionally-split approach: the hydrodynamic equations were solved first along one coordinate grid direction, then the other at each time step.

An equation of state was employed that assumed full ionization and included contributions from radiation and ideal gas pressure:

$$P = \frac{1}{3}aT^4 + \frac{k_B T \rho}{m_p \mu} \quad (1)$$

$$E = \frac{aT^4}{\rho} + 1.5 \frac{k_B T}{m_p \mu} \quad (2)$$

where P is the pressure, a is the radiation constant, k_B is Boltzmann’s constant, T is the temperature, ρ is the density, m_p is the proton mass, μ is the mean molecular weight, and E is the energy. Although the outer regions of the remnant may not always be fully ionized, the regions where Rayleigh-Taylor mixing takes place are. Exploratory simulations performed in one dimension with

FLASH using a Helmholtz equation of state were identical to one-dimensional simulations performed with the perfect gas and radiation equation of state used in the simulations presented in this paper. These one-dimensional simulations were only run to 2×10^4 seconds. At later times, the density is low enough that the Helmholtz equation of state no longer applies.

The code was configured to use pressure, density, ^4He , and ^{16}O as its refinement variables. An error estimate for a block was computed using the second derivative of the chosen refinement variables. If the estimated normalized error in one or more of these variables was greater than a given value, regions were refined until a normalized error is reached that is less than the acceptable value or the maximum level of refinement is reached. Regions of the simulations with steep gradients in one or more of these variables were likely to be refined. If the normalized error estimate was below a certain value, i.e., the absolute value of the second derivative of one or more variables was small, then the region was ‘‘de-refined’’.

2.3. Modifications to the FLASH Code

The FLASH2.5 release was customized to include a module that inserts a roughly circular zero-gradient inner boundary around the origin. This prevented infalling matter near the origin in the simulations from backing up and affecting the outer regions. Matter was allowed to fall through the zero-gradient, quasi-circular boundary at the center of the model and accumulate on the point mass at the origin. If the radius for the inner boundary passed through one of the inner zones, the zones interior to that zone were set to be duplicates of the zone on the boundary. While the Cartesian nature of the axisymmetric coordinate system meant that the inner boundary was only as close to circular as one can reproduce with square components, it did not introduce a significant amount of error into the calculation. The inner boundaries were chosen to be within the sonic radius, ensuring that small numerical errors at the interior boundary did not accumulate and affect the flow of fluid upstream from the boundary. The sonic point moved outward, not inward, as the simulation time progressed, so the inner boundary was always within the sonic radius. The falling temperature caused the sound speed to decline with time, while the velocity near the inner boundary increased with time. The gravitational potential resulting from this point mass was updated and added to the gravitational forces computed by the multipole solver at each time step.

A module was also included that locally deposited energy from radioactive decay of ^{56}Ni to ^{56}Fe . The amount of energy

$$dE_{56\text{Ni}} = \lambda_{56\text{Ni}} X_{56\text{Ni}} e^{-\lambda_{56\text{Ni}} t} * q(^{56}\text{Ni}) \quad (3)$$

The decay rate of ^{56}Ni , $\lambda_{56\text{Ni}}$, is $1.315 \times 10^{-6} \text{ s}^{-1}$, and the amount of energy released per gram of decaying ^{56}Ni is $q(^{56}\text{Ni})$, for which we took the value $2.96 \times 10^{16} \text{ erg g}^{-1}$. $X_{56\text{Ni}}$ is the fraction of ^{56}Ni in the block. The amount of ^{56}Co at a given time could be found as a function of the amount of initial ^{56}Ni by

$$X_{56\text{Co}} = \frac{\lambda_{56\text{Ni}}}{\lambda_{56\text{Co}} - \lambda_{56\text{Ni}}} X_{56\text{Ni}} (e^{-\lambda_{56\text{Ni}} t} - e^{-\lambda_{56\text{Co}} t}) \quad (4)$$

so that the energy deposition rate from ^{56}Co as a function

of time was given by

$$dE_{56\text{Co}} = \frac{\lambda_{56\text{Ni}}}{\lambda_{56\text{Co}} - \lambda_{56\text{Ni}}} X_{56\text{Ni}} (e^{-\lambda_{56\text{Ni}}t} - e^{-\lambda_{56\text{Co}}t}) \lambda_{56\text{Co}} * q(^{56}\text{Co}) \quad (5)$$

We assumed a decay rate for ^{56}Co , $\lambda_{56\text{Co}}$, of $1.042 \times 10^{-7} \text{ s}^{-1}$, and an energy per gram of decaying ^{56}Co , $q(^{56}\text{Co})$, for which we took the value of $6.4 \times 10^{16} \text{ erg g}^{-1}$.

2.4. Calculations

The supernova models were evolved with KEPLER to the point where all explosive nuclear burning had ceased and the reverse shock had just begun to form. This occurred at 10^3 s and 10^4 s for 15 and 25 M_{\odot} stars of solar composition, and at 25 s and 100 s for 15 and 25 M_{\odot} stars of primordial composition, respectively. At these times, the one dimensional models from KEPLER were mapped onto a two-dimensional axisymmetric grid and evolved forward in time with the FLASH code. A similar simulation of Model s25A was also performed using a progenitor evolved to 10^3 seconds with KEPLER before being mapped to FLASH. No significant difference in the later evolution of s25A models evolved to 10^3 seconds and 10^4 seconds was observed. Only one quadrant of the star was carried in the calculation, enforcing symmetry about the left y - and bottom x -axes, while allowing material to leave the grid through a zero-gradient boundary at the right y - and top x -axes.

An enhanced flow was observed along the x - and y -axes. This flow was not large in comparison with the rest of the simulation, but it was present, as can be seen in Figures 7 - 6. This is a well-documented artifact of the dimensionally-split approach to solving the hydrodynamic equations. It did not substantially influence the evolution of the simulations presented here.

Perturbations arising from a Cartesian grid are also inevitable. In order to quantify these grid effects, we performed simulations of all stars with a random perturbation in velocity with a maximum amplitude of 0.5% and 2.0%. We also performed simulations with no additional perturbation. We found that perturbations of 2.0% in velocity had a clear effect on the initial scale of the Rayleigh-Taylor instability, increasing the amplitude and scale of the first instabilities to form. This effect is shown for s15A in Figure 1. The case of 0.5% random perturbations to the velocity results in a scale for the initial Rayleigh-Taylor instabilities that is roughly equivalent to the case where the only perturbations were those arising from the Cartesian grid itself. Other models had similar resolution, such that grid perturbations were roughly equivalent to velocity perturbations of 0.5% and velocity perturbation of 2.0% had a noticeable effect on the initial scale of the instability. Perturbations arising from the grid were no larger than 2%, well within the regime of perturbations expected to arise from convection.

Because the zD-series models were more compact than sA-series models, the reverse shock reached the centers of zD models faster than in the sA models. This had the effect of shutting off mixing in the zD-series before the Rayleigh-Taylor instability had time to become fully non-linear (see also Herant & Woosley 1994). The initial perturbations had a greater effect on the final state of the zD simulations, while the initial perturbation scale and

spectrum are washed out in the sA models as a result of their longer mixing times. A simulation with random velocity perturbations of 5% was performed for Model z25D.

Models were initially mapped onto the two-dimensional grid such that their inner iron cores were resolved with at least 4 blocks of 16 zones each. This was sufficient to ensure that the rest of the star was accurately resolved. As the simulation progressed and the model stars expanded, the maximum refinement level of the simulation was turned down, so that the model star was always resolved at about the same percentage of the radius of its inner core of ^4He and heavier isotopes. This is the region where Rayleigh-Taylor mixing takes place. The star expands homologously, ensuring that all regions will be adequately resolved.

The solar composition models were mapped onto a grid $5 \times 10^{14} \text{ cm}$ on a side. The zero-metallicity stars were mapped onto a grid $1.4 \times 10^{14} \text{ cm}$ on a side. The portion of the grid outside the original KEPLER model was initialized with a density proportional to r^{-2} . Simulations with an outer density proportional to $r^{-3.1}$ was also performed for Models s15A, s25A, and z25D. These density profiles span the realistic range of smooth density distributions outside real stars. No difference in the final profiles for density, temperature, pressure, or composition was found between models with different outer density profiles. The density profile of the surrounding material therefor has no effect on the amount of Rayleigh-Taylor mixing that goes on inside the star, provided very little mass as a proportion of the original mass of the star is swept up in the first days of the explosion. The amount of mass added to the grid from ambient density was $< 2\%$ for all models.

Calculations were run at least until the Rayleigh-Taylor fingers had ceased to move with respect to the mass coordinate of the star. This happened 2 hours after core bounce for Model z15D, 4 hours after core bounce for z25D, and 7 days after core bounce for the s15A and s25A models. All models were followed to 10^6 seconds, long after Rayleigh-Taylor mixing had frozen out in the zero metallicity stars, but long enough that infall though the inner boundary had reached an asymptotic stage and the final remnant mass from these two-dimensional simulations could be determined.

3. RESULTS

Figure 2 shows the evolution of the stable and unstable regions of the models, and the position in mass coordinate of the forward and reverse shocks. A reverse shock forms when the outgoing shock encounters a region of increasing ρr^3 (Herant & Woosley 1994; Woosley & Weaver 1995). When the shock encounters a density profile that falls off with a flatter slope than $\propto r^{-3}$, i.e. when it encounters a region of increasing ρr^3 it decelerates. The deceleration of the forward shock front reverses the direction of the pressure gradient, which slows down the layers interior to the shock, as well. Shocked material piles up and forms a high density post-shock shell. The reverse shock forms at the inner boundary of the high-density shell of decelerated matter and propagates down into the star, toward its center, slowing down the deeper, inner layers of the star (Kifonidis et al. 2003). The deceleration of the shock creates a steep pressure gradient in

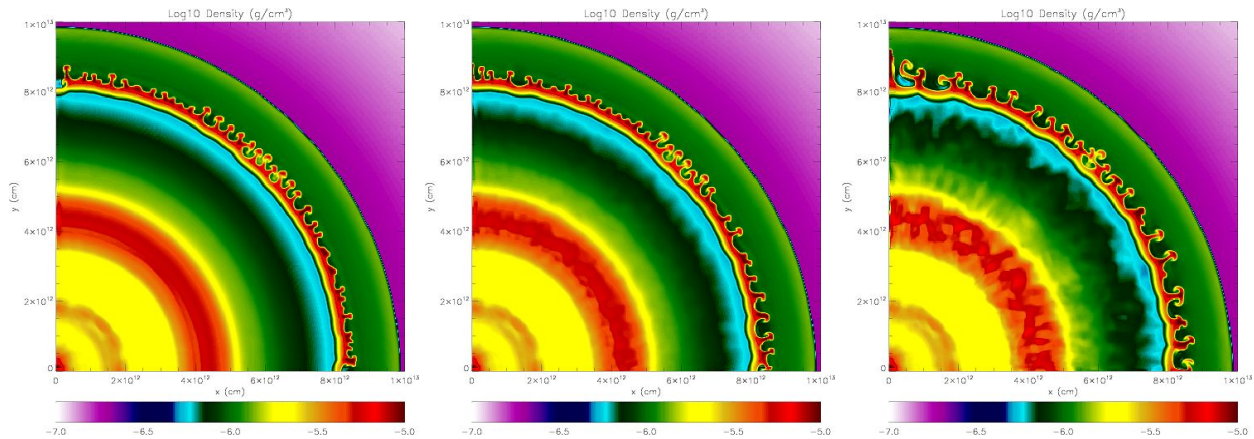


FIG. 1.— Influence of perturbations on the initial scale of the instability. Panel (a): no additional perturbation. Panel (b): random perturbations of 0.5% applied to velocity. Panel (c): random perturbations of 2.0% applied to velocity. Panel (a) and (b) show instability growth on nearly the same scale, implying that grid perturbations were on the order of 0.5%. The scale of the instability in panel (c) is noticeably larger, showing that perturbations from the grid are no larger than 2.0%. The other models presented in the current paper, not shown, are nearly the same. The initial scale and spectrum of the instability is washed out after the instability becomes nonlinear in the solar stars.

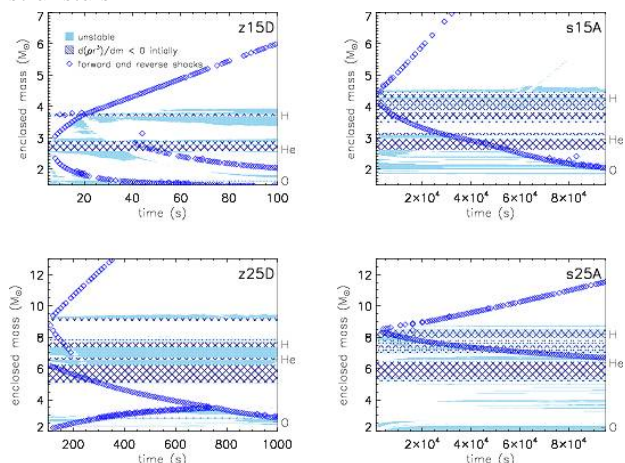


FIG. 2.— Stability evolution for the first $\approx 5\%$ of simulation time. Left axes show the location of the base of the shell indicated. Note different time and mass axes scale between the models. The reverse shock takes far longer to propagate back for solar composition than for Pop III stars. A greater portion of mass in the solar stars is RT unstable, leading to more mixing in these stars.

the opposite direction to the existing gravitational and density gradients. This pressure gradient can overwhelm the gravitational gradient, and in doing so triggers the formation of Rayleigh-Taylor instabilities in the material. The Rayleigh-Taylor instability develops until the reverse shock has passed by, at which point the material becomes stable again, and the instabilities cease to grow exponentially. Figure 2 covers the period of time from when the models were first mapped to FLASH to slightly beyond the time when the Rayleigh-Taylor instability fingers began to grow.

Figure 2 shows that the Rayleigh-Taylor instability had far more time to develop in the solar composition models than primordial composition models. The zero-metallicity models, particularly Model z15D, were far more compact than their solar metallicity counterparts. The reverse shock took only ≈ 100 seconds to reach the center of Model z15D, leaving very little time for the Rayleigh-Taylor instability to grow. This is reflected in the low degree of mixing seen in Figure 4, which shows the final distribution of isotopes as a function of mass

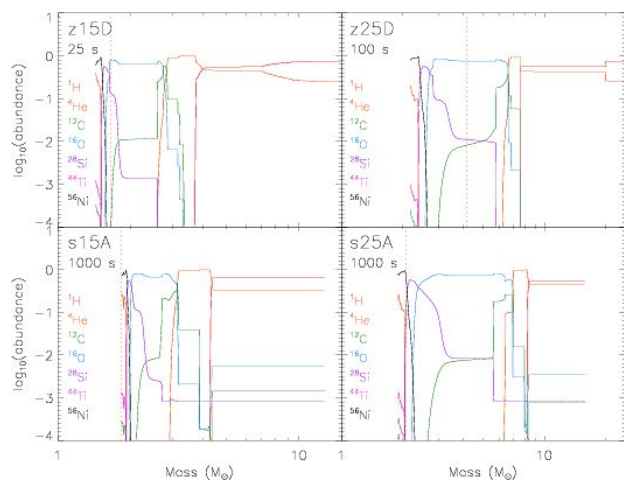


FIG. 3.— Distribution of isotopes just after core bounce as a function of mass coordinate. The dotted vertical line shows the position of the mass cut—matter to the left of this line will fall back onto the star. Without mixing, no ^{56}Ni escapes from stars of primordial composition, while most of the ^{56}Ni core is expelled from the solar composition supernovae.

for all stars. The original structure of these stars can be seen in Figure 3. Two-dimensional snapshots of mixing are shown in Figure 5, which shows the density structure of the entire star, and Figure 9, which shows the isotopic composition of the mixed region at the center of the model. In Model z25D, the reverse shock took longer, about 10^3 seconds, to reach the center of the star, allowing the RT instability to grow for a longer period of time. Figure 2 shows an unstable band between the $^4\text{He}/^{12}\text{C}-^{16}\text{O}$ shell boundary, and that was indeed the place we saw mixing in these models. More mixing in z25D than z15D can be seen in Figures 4, 6, and 10.

Solar composition models were about 50 times larger in radius than their primordial composition counterparts, and correspondingly less dense. The reverse shock took longer to form and 10^5 and 2×10^5 seconds to propagate back to the mass-coordinate origin for Models s15A and s25A, respectively. This was about 100 times longer than for Model z25D, giving the Rayleigh-Taylor instability more time to develop. Additionally, a wider range of re-

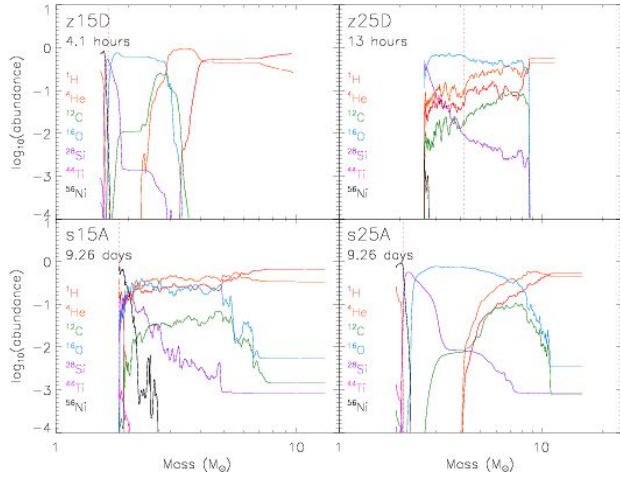


FIG. 4.— Distribution of isotopes after mixing has ceased. Note that we find almost no difference between this distribution and the initial configuration for Model z15D. Mixing is confined to the O-He shells for Model z25D. Mixing has penetrated the Si/O layer for Model s15A.

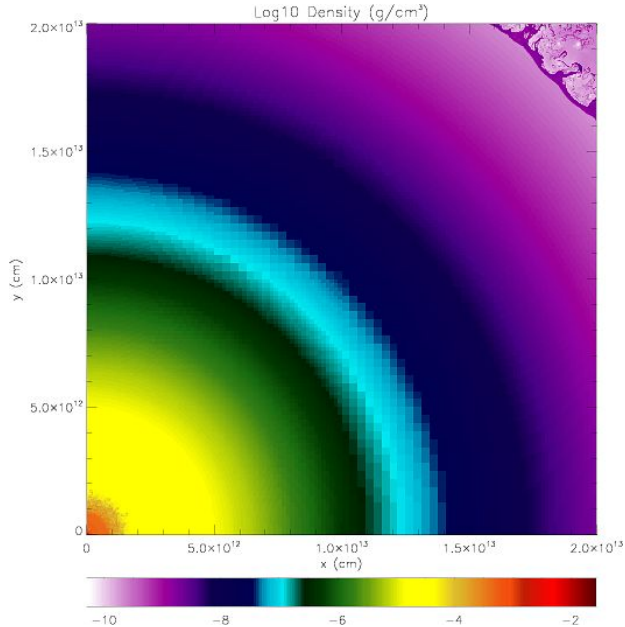


FIG. 5.— Log(density) snapshot of Model z15D after mixing has ceased. The RT instability visible in the upper right hand corner is most likely a result of the artificial outer density profile. It represents the outer layer of the star. The mixed inner layer extends only about 1/10 of the radius of the star, covering a much smaller region than in the solar models.

gions between and including the ${}^4\text{He}$ and Si+S shells were unstable than in the zero metallicity counterparts. Figure 2 implies that the solar metallicity stars were mixed to a greater degree than stars of zero metal initial composition. Figures 7 and 8 show that about half the solar composition stars were mixed, compared to only about 1/10 of the zero metallicity stars.

3.1. Infall

Infall is as important as mixing for determining the final yield of a supernova. For a freely expanding supernova remnant, the rate at which mass accretes onto the black hole or neutron star at the center of the explosion is given by $\dot{M} \propto t^{-5/3}$ (Chevalier 1989). It takes super-

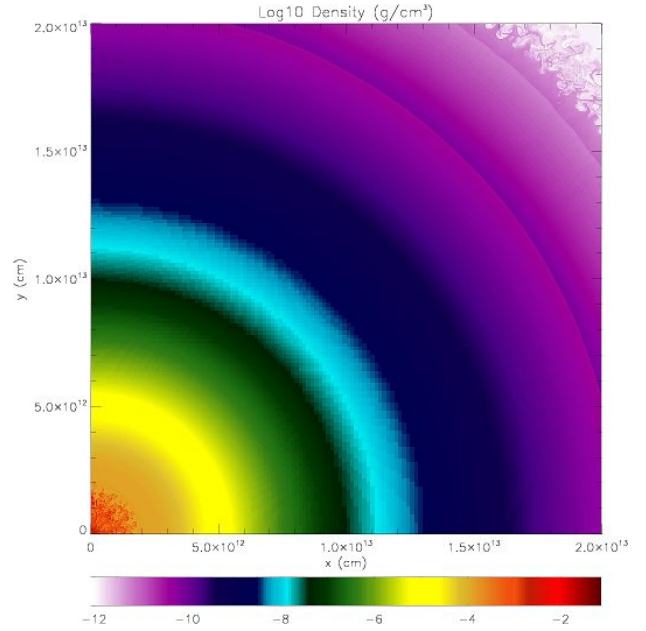


FIG. 6.— Log(density) snapshot of Model z25D after mixing has ceased. Like Model z15D, a small portion of the star is mixed when compared to the corresponding model of solar composition. The RT instabilities visible in the upper corner formed at the boundary of the star with an artificial density background.

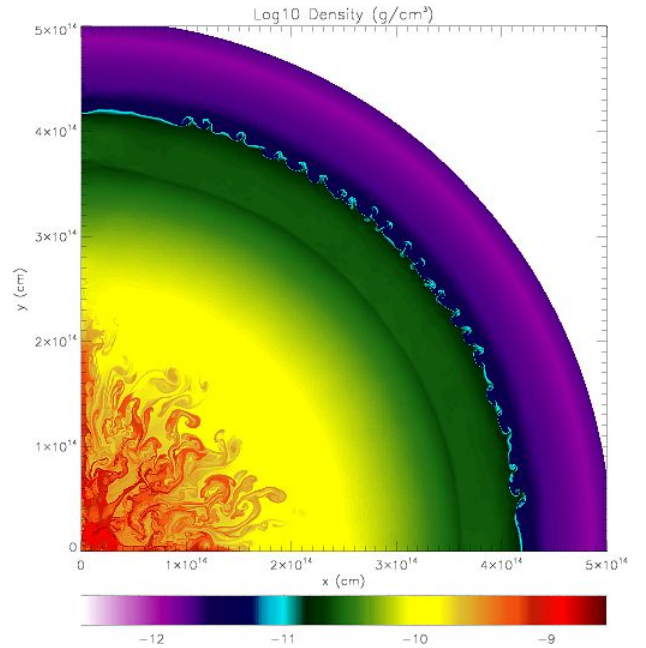


FIG. 7.— Log(density) snapshot of Model z25D after mixing has ceased. The Rayleigh-Taylor instability that began at the O/He interface has mixed the inner layers of the star down to the iron core. The flow visible along the y-axis is a result of dimensional splitting in the hydrodynamic solver.

nova explosions on the order of 10^6 seconds to reach this asymptotic, freely expanding stage, at which time it is possible to determine the final mass of the stellar remnant by extrapolating from the asymptotic infall rate. Our final remnant masses are compared with those found with one-dimensional calculations carried out by Zhang et al. (2008) with the PANGU code in Figure 13.

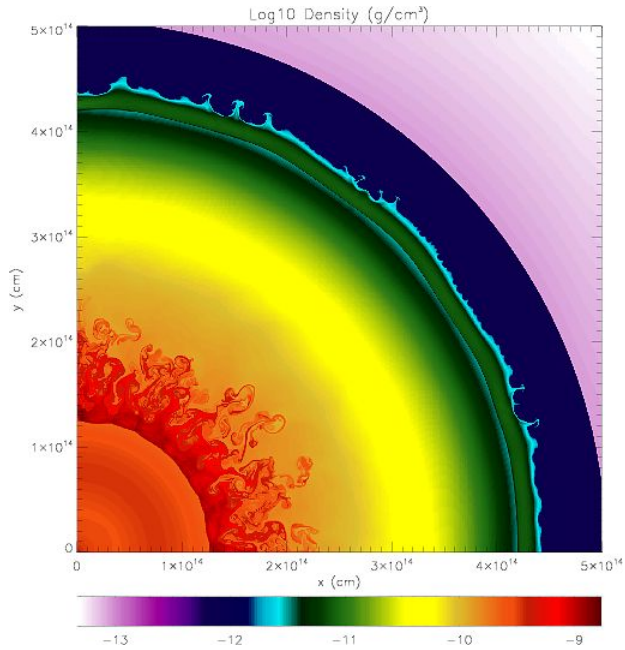


FIG. 8.— Log(density) snapshot of Model s25A after mixing has essentially ceased. The Rayleigh-Taylor instability that began at the O/He interface has not penetrated through the thick ^{16}O shell, as it had with model s15, where the shell was thinner (Figure 7.)

PANGU is a one-dimensional hydrodynamics code based on the second-order semi-discrete finite difference central scheme of Kurganov & Tadmor (2000). Time evolution was carried out by a third-order total variation diminishing Runge-Kutta method (Shu & Osher 1989). Zhang et al. (2008) simulated the explosions of stars in the Woosley & Heger (2007) and Heger & Woosley (2008) surveys. Using this one-dimensional code, the authors followed the evolution of the supernova remnant out to 10^6 seconds, to the time at which the accretion rate onto the central remnant had reached an asymptotic dependence on time and the final remnant mass could be determined.

Our final remnant masses showed good agreement with the PANGU results for all Models except Model z25D, as shown in Figure 13. The shape of the infall curves for our stars, as shown in Figure 13, match the PANGU results well, though the remnant masses from FLASH are larger except in the case of s25A. Model s25A was mapped to FLASH after 1×10^4 seconds of evolution in KEPLER. Although this does not alter the final mixed state of the star, it does alter the amount of mass that accumulates at the inner boundary, since most of the infall occurs during the first 10^4 seconds, when the star was still being evolved forward with the Lagrangian code KEPLER. Both 15 solar mass models are in good agreement with the PANGU results. z25D shows the most deviation, most likely because this model experienced the most fall back of any of the models studied here. We were unable to replicate the fine resolution employed by a one dimensional code, and that is almost certainly the reason for the enhanced infall mass. The initial remnant mass in 2D was sufficiently larger than the 1D remnant mass that the additional force it exerted on the surrounding material was large enough to cause additional infall. This led to a larger remnant, causing a mild runaway effect. While the remnant mass obtained with FLASH for Model z25D is

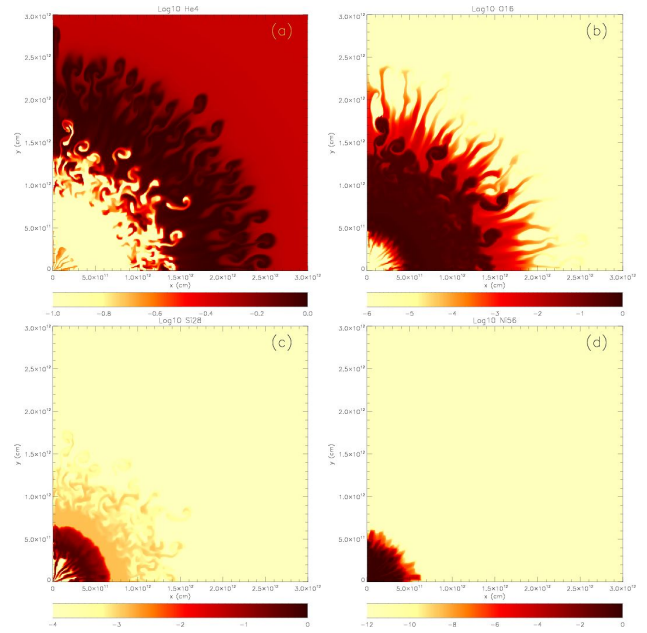


FIG. 9.— Final distribution of isotopes in the inner core of Model z15D. Note that the mixed region extends only to about 1/10 of the radius of the star—a much smaller proportion than in the solar metallicity stars. Pictured is the run with a 2% percent perturbation in velocity. The Rayleigh-Taylor instabilities have had a shorter time to grow, and so have retained more of their original shape, than in the solar metallicity models.

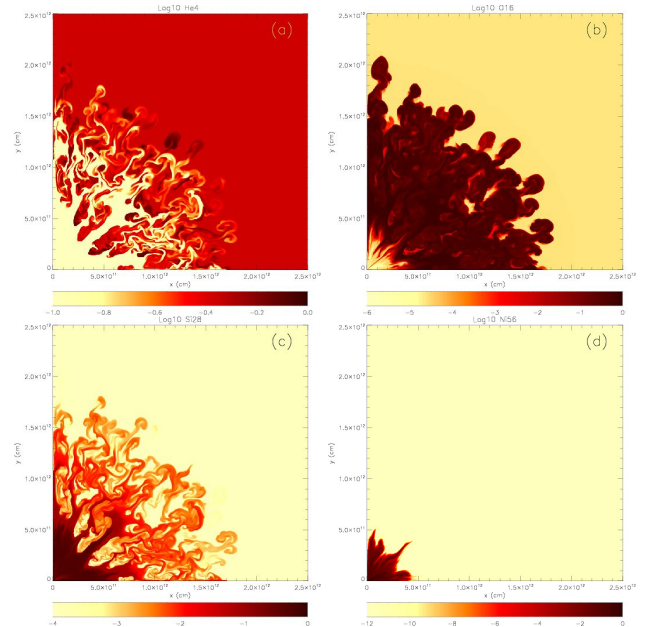


FIG. 10.— Final distribution of isotopes in the inner core of model z25D with a 5% perturbation in velocity. Note the mixed region goes out to only about 1/10 of the radius of the star—a much smaller proportion than in the solar metallicity stars, although the mixed region is greater and the initial scale of the perturbation is less visible than in Model z15D. The reverse shock took longer to pass though Model z25D than Model z15D.

likely inaccurate, Rayleigh-Taylor mixing in this star has stopped by 2×10^4 seconds, at which point the remnant mass in the FLASH simulation was not significantly larger than that in the PANGU simulation. It is unlikely that increased infall has had a significant impact on the evolution of the Rayleigh-Taylor instability, so the mixing

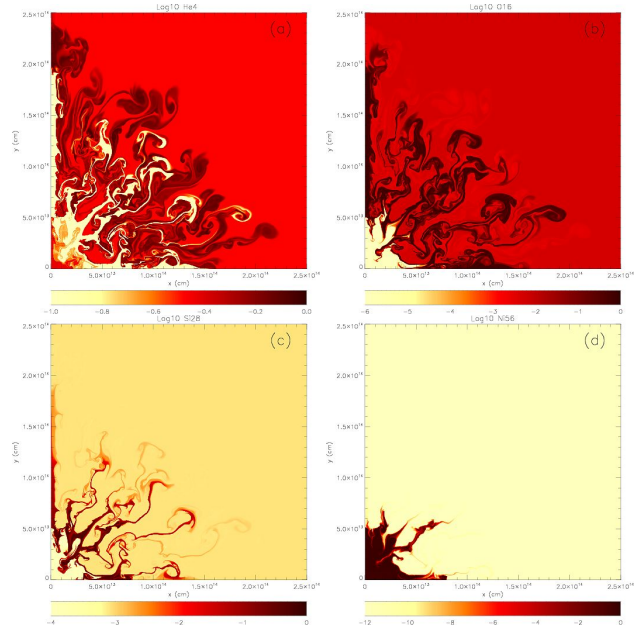


FIG. 11.— Final distribution of isotopes in the inner core of Model s15A. The helium, oxygen, and silicon shells have been disrupted by the Rayleigh-Taylor instability, which has mixed ^{56}Ni out of the core and ^1H all the way in to the inner layers. Model s15A is more completely mixed than any other model presented in this paper, because of both the long timescale for the reverse shock and a thinner oxygen layer.

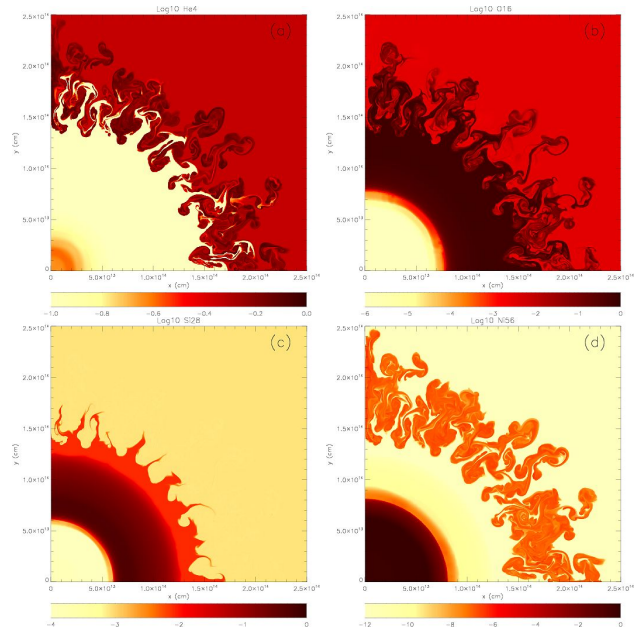


FIG. 12.— Final distribution of isotopes in the inner portion of Model s25A. The ^4He layer has been completely disrupted, though the RT instability has not penetrated past the ^{16}O layer. The ring of ^{56}Ni visible was formed by explosive nuclear burning. ^{56}Ni has not been mixed out of the center of the star, and the ^{28}Si layer is only marginally effected by the Rayleigh-Taylor instability.

results remain sound.

3.2. Perturbations

Random perturbations of amplitude 0.5% and 2% of the original velocity profile were added to the initial model for the solar composition models, as described in § 2.2. Random perturbations of 2% were added to the

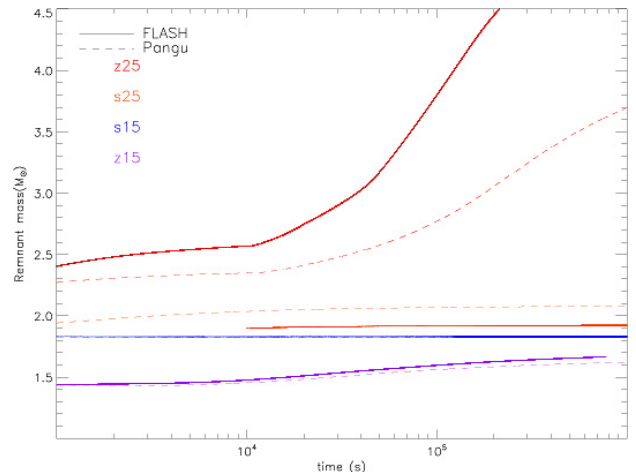


FIG. 13.— Comparison of infall rates through the inner boundary for 1-d PANGU and 2-d FLASH Eulerian codes. For all stars except Model s15A, FLASH overestimates the initial infall rate, which is reflected in a larger remnant mass. This is due to limited resolution at the origin in the FLASH code. The shape of the FLASH infall curves matches the shape of those curves in PANGU. The exception is Model z25D, which shows a dramatic departure from the shape of the PANGU curve at later times. This is probably because the extra remnant mass is large enough to effect the infall rate through the inner boundary.

zero-metal stars, and an additional simulation with an initial perturbation of 5% was performed for Model z25D. Perturbations of 0.5% produce an original size scale for the Rayleigh-Taylor instabilities that is about the same size as those arising for the non-perturbed case, while the 2% perturbations result in a larger initial scale for the instability, implying that grid perturbations for these models are between 0.5% and 2%, as shown in Figure 1. The Rayleigh-Taylor instabilities can grow for at least as long as the reverse shock takes to reach the origin. The instabilities in the solar metallicity stars can grow for many e -folding times, a long enough time to wash out the initial scale and spectrum of the instabilities. The final states of the perturbed models appear essentially identical to the unperturbed models. The distribution of the isotopes in both velocity (Figures 16 and 17) and mass space (Figures 20 and 21) has no systematic correlation with the magnitude of the initial perturbation for solar metallicity stars. The scale of the perturbations one would expect in a real star is set by the magnitude of the convective velocities, which are on the order of 0.5% of the total velocity.

Perturbations for the zero-metallicity case have a greater effect on the final amount of mixing in these stars. Larger perturbations lead to a larger size scale for the initial Rayleigh-Taylor fingers, which allows them to grow more quickly before the reverse shock passes them and the pressure gradient is no longer opposite the density gradient. In these models, the Rayleigh-Taylor instabilities cannot grow for many e -folding times, and so the initial scale of the perturbations matters. This can be seen in Figures 18 and 19, which show the final distribution of isotopes as a function of enclosed mass for different amounts of perturbation. The final amount of mixing is set by the size scale of the initial perturbation. The amount of mixing determines the distribution of isotopes with velocity, as well, as shown in Figures 14 and 15. ^{16}O and ^4He are the most affected. The distance

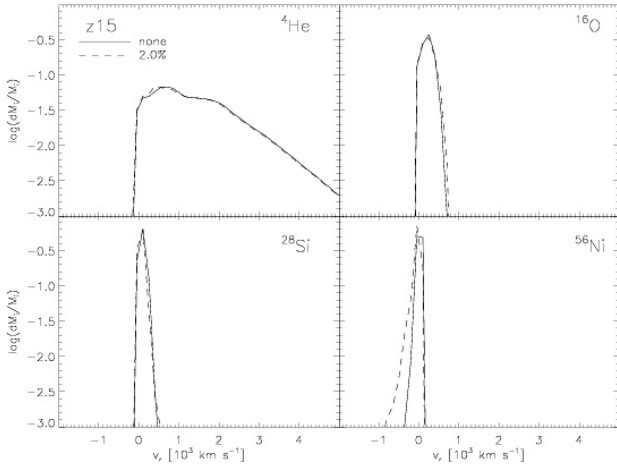


FIG. 14.— Mass fraction of chemical isotopes as a function of radial velocity for Model z15D for different perturbations. Larger initial perturbations lead to wider distributions. These differences effect about 10% of a given isotope.

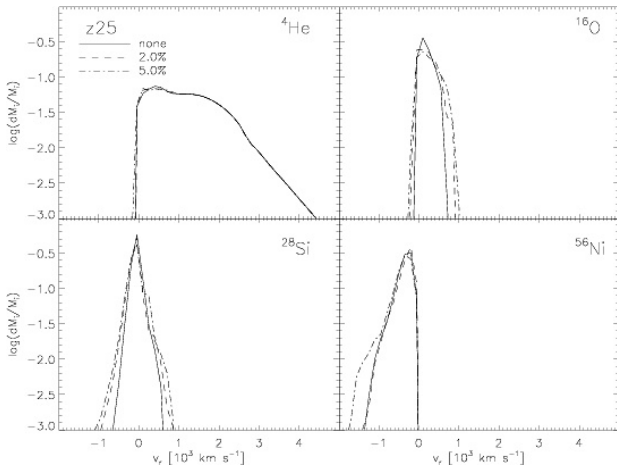


FIG. 15.— The same as Figure 14, but for model z25D. As with Model z15D, a greater perturbation results in slightly enhances negative velocities, especially for ^{56}Ni .

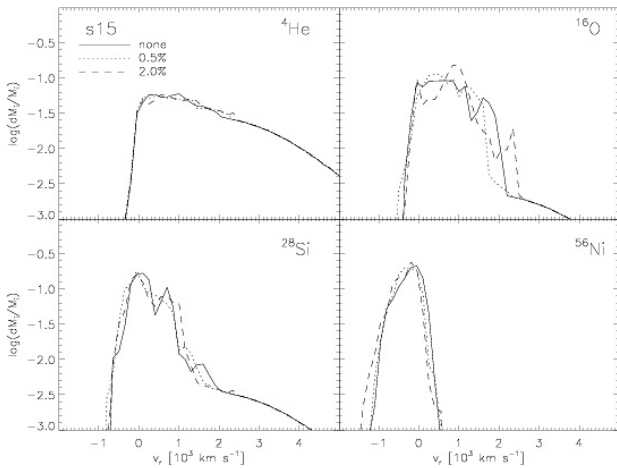


FIG. 16.— Mass fraction of chemical isotopes as a function of radial velocity for model s15A. Differences between the models are larger than for Model s25A (see Figure 17, but are not systematic with perturbation, and become significant only below mass fractions of around 5% of the mass of ^{16}O and ^{28}Si .

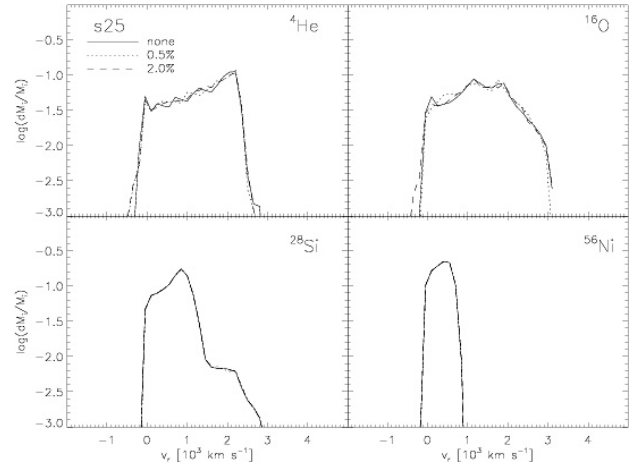


FIG. 17.— Mass fraction of chemical isotopes as a function of radial velocity for Model s25A with different perturbations. There are only small differences, and the differences are not systematic with the amount of perturbation imposed on the initial model.

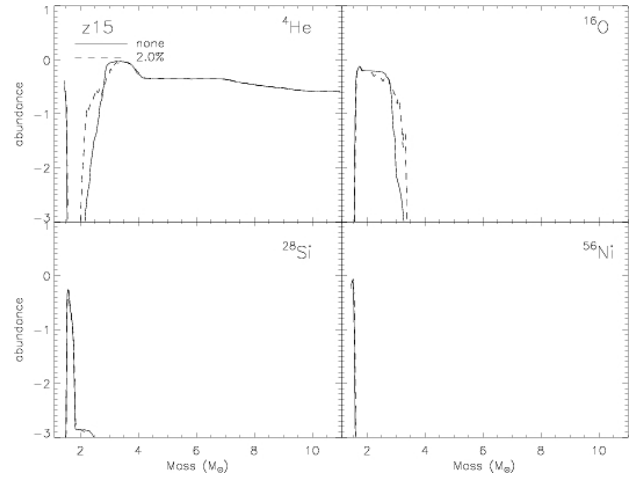


FIG. 18.— Isotopic distribution as a function of mass for Model z15D with different initial perturbations. A larger perturbation leads to more mixing.

in mass space over which these isotopes are mixed varied by around $1 M_{\odot}$ for the perturbed models.

3.3. Velocity Distribution

The velocity distribution of chemical isotopes is shown in Figure 22. ^{44}Ti was mixed to relatively high velocities in our solar metallicity stars. The solar stars show ^1H and ^4He at high velocities of $4 \times 10^3 \text{ km s}^{-1}$. These isotopes are also mixed all the way to the core of the solar metallicity stars, and some fraction of them reaches negative velocities of less than $-0.5 \times 10^3 \text{ km s}^{-1}$. In Model s15A, where the most mixing takes place, we see ^{16}O and ^{12}C mixed out to $2 \times 10^3 \text{ km s}^{-1}$ in velocity space. ^{56}Ni does not reach the high velocities observed in 1987A. Model s15A shows a peak in the ^{56}Ni velocity at $\approx 0 \text{ km s}^{-1}$, with a tail extending to $0.7 \times 10^3 \text{ km s}^{-1}$. Model s25A shows slightly higher velocities, with the ^{56}Ni distribution peaking at around $0.4 \times 10^3 \text{ km s}^{-1}$ and reaching out to $0.9 \times 10^3 \text{ km s}^{-1}$. These higher velocities for ^{56}Ni are probably due to smaller amounts of fallback in this star.

The zero metallicity stars show lower velocities overall. At the time they exploded as supernovae, these stars

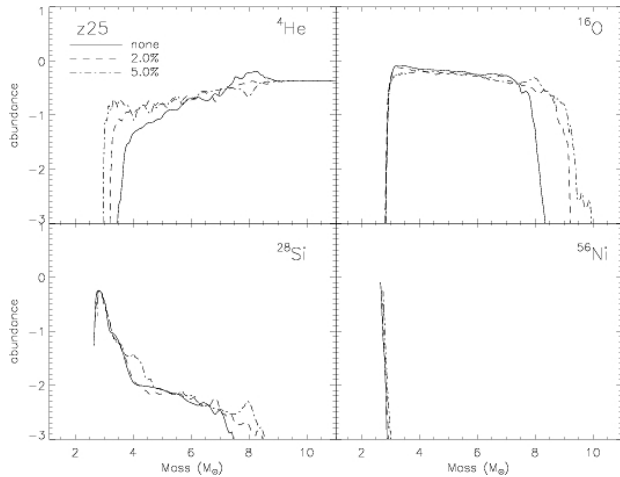


FIG. 19.— Isotopic distribution as a function of mass for Model z25D with different initial perturbations. The distribution changes with the level of perturbation—larger perturbations lead to more mixing in a systematic way, and the difference between different perturbations is visible at the level of 50% mass fraction of ${}^4\text{He}$ and ${}^{16}\text{O}$, much larger than in the more non-linear solar metallicity stars.

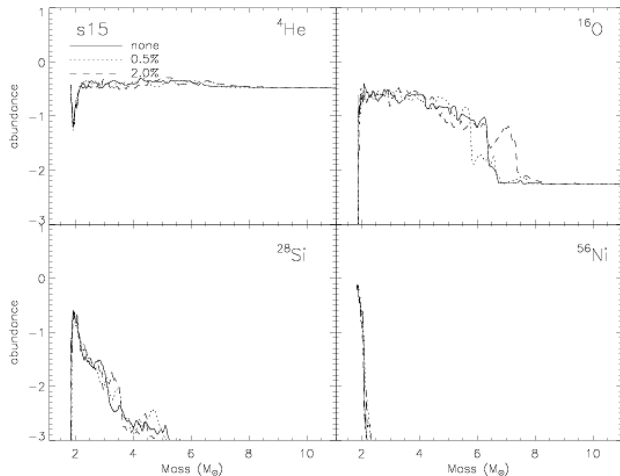


FIG. 20.— Isotopic distribution as a function of mass for Model s15A with different initial perturbations. The isotopic distribution is not systematic with the amount of perturbation. ${}^{16}\text{O}$ shows the greatest change, but only at mass fractions below 10%.

were more compact than solar composition stars. The supernova shock ran into a higher fraction of the total mass of the star at an earlier time. In neither zero metal model were the heavier isotopes mixed out to higher velocities than $1 \times 10^3 \text{ km s}^{-1}$, but in Model z15D the velocities of ${}^{56}\text{Ni}$ and ${}^{44}\text{Ti}$ had slight positive components, whereas in Model z25D the velocity distribution of these isotopes was almost entirely negative. No ${}^{56}\text{Ni}$ or ${}^{44}\text{Ti}$ escape from Model z25D.

Kifonidis et al. (2006) in their 1987A-type models, which had a metallicity and mass intermediate to the stars studied in this paper, saw a well-mixed heavy element core. The velocity profiles for isotopes from ${}^{16}\text{O}$ to the iron group were very similar. Because we did not see the iron core of our solar metallicity stars mixed to the degree seen in Kifonidis et al. (2006), our ${}^{56}\text{Ni}$ had a slower velocity distribution, while lighter isotopes, from ${}^{44}\text{Ti}$ and ${}^{28}\text{Si}$ and lighter, were skewed towards higher velocities.

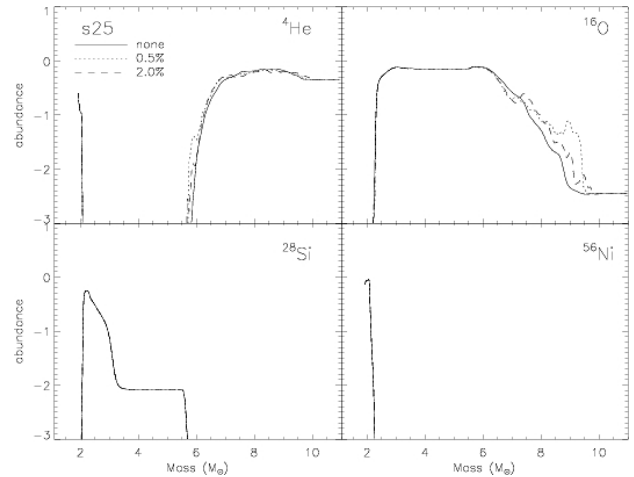


FIG. 21.— Isotope distribution as a function of mass for Model s25A with different initial perturbations. Where the distributions of isotopes are different, they are not systematic with perturbation. Differences between the runs are also small, and only become obvious for ${}^{16}\text{O}$, with oxygen concentrations are less than 10%.

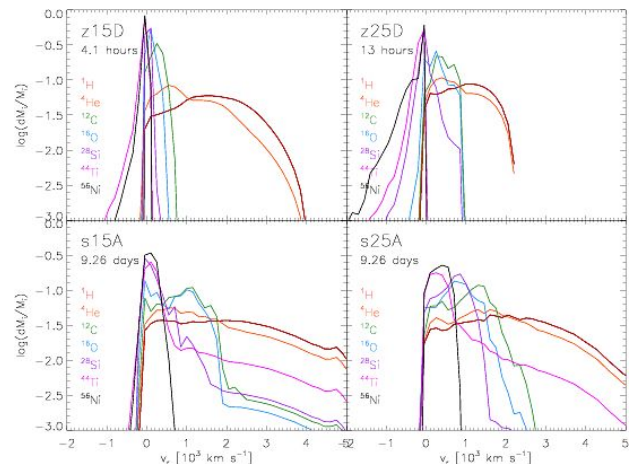


FIG. 22.— Mass fraction of chemical isotopes as a function of velocity for Models s15A and s25A at $t = 9.26$ days and z15 and z25 at $t = 2$ and 4 hours, respectively. Negative velocities indicate material falling toward the point mass at the center of the star. Virtually no iron-peak elements escape from the primordial composition stars, and their velocity distributions are smaller than the solar models. The peaks in the velocity distribution for ${}^{56}\text{Ni}$ for the solar stars are not high enough to match what was observed in 1987A, but are consistent with previous studies of mixing in RSGs.

The ${}^{56}\text{Ni}$ velocities observed in the zero-metallicity models were lower than those produced in earlier attempts at modeling SN 1987A, as well. The maximum iron-peak velocities obtained was on the order of 1300 km s^{-1} (Arnett et al. 1989; Hachisu et al. 1990; Fryxell et al. 1991; Mueller et al. 1991; Herant & Benz 1991). In particular, Herant & Benz (1991) found that following the radioactive decay of ${}^{56}\text{Ni}$ and ${}^{56}\text{Co}$ increased the velocity of iron-peak elements slightly, but not enough to match observations of SN 1987A. Our iron-peak velocities were lower still. This was partly due to the large amount of fallback experienced by the primordial composition models. Most of the ${}^{56}\text{Ni}$ fell through the inner boundary of our zD-series simulations before it had time to power a nickel bubble like those seen in SPH simulations of SN 1987A (Herant & Benz 1991). Our progenitors were also more compact, with smaller helium cores, than the pro-

genitor models for 1987A used in the above simulations. ^{56}Ni was not mixed out to the the high velocities seen in SN1987A. Utrobin (2004) report that ^{56}Ni was mixed out to at least $2.5 \times 10^3 \text{ km s}^{-1}$. In no model did we see nickel at these high velocities. Significant low-order asymmetry in the explosion is probably necessary to reach ^{56}Ni velocities high enough to match observations.

In their 1994 paper on mixing in supernovae with red supergiant progenitors, which employed progenitor models similar to the s15A and s25A progenitor models in this survey, Herant and Woosley found a similar distribution of isotopes in velocity space to the results presented here. They found a peak in the velocity distribution of ^{16}O at around $1.4 \times 10^3 \text{ km s}^{-1}$ for their $25 M_{\odot}$ star, we see one at around $1.1 \times 10^3 \text{ km s}^{-1}$. We see oxygen mixed out to slightly higher velocities in our model s15A than are given in Herant & Woosley (1994). Their models show no negative velocities, which is probably a result of the SPH technique employed, which did not allow for accretion onto a sink particle at the center of the simulation.

3.4. Yields

The yields of our stars are greatly affected by the amount of fallback and degree of mixing induced by Rayleigh-Taylor instabilities. For models that experienced a great deal of fallback, as in case of the zero-metallicity models, mixing is of crucial importance in determining the final yields. Figure 3 shows the original distribution of isotopes in the four stars studied in this paper. The distribution of isotopes after all mixing has ceased is shown by Figure 4. As Figure 4 and Figures 9 and 10 show, layers interior to oxygen in the zero-metallicity stars have not mixed appreciably. A far larger portion of the solar metallicity stars has been mixed together. The Rayleigh-Taylor instability has penetrated as far as the ^{56}Ni core of model s15A, completely disrupting the exterior shells. This can be seen in Figure 11. Figure 12 also shows that Model s25A experienced more mixing than Model z25D (Figure 10), but not quite as much as Model s15A. The lack of mixing into the interior layers of the zero-metallicity models means that very little of the silicon shell, and virtually none of the elements interior to this shell are mixed out. This, coupled with a large amount of infall, means that these Pop III stars expel almost no ^{56}Ni .

To eliminate the possibility that the absence of Rayleigh-Taylor induced mixing at the edge of the ^{56}Ni shell in Models z15D and z25D could have been due to mapping to two dimensions at too late a time we performed four simulations of the interior of Model z25D with an inner boundary of $1 \times 10^9 \text{ cm}$, an order of magnitude smaller than that used to simulate the star in the main simulations presented in this paper. These simulations were run at ten times the resolution of the simulations presented in § 2.4. KEPLER models were mapped in 10 and 40 seconds after bounce. To maintain consistency with the simulations that used a mapping from KEPLER at 100 s after bounce, we initially used a reflecting condition at the inner boundary, which did not allow infall. At 100 seconds after bounce for all of these high resolution models the inner boundary condition was changed to be zero-gradient. No Rayleigh-Taylor instabilities are seen to develop by $1 \times 10^3 \text{ s}$ of simulation time, the point when

the instabilities are clearly defined and growing along the C-O/He interface. Perhaps the perturbations from the Cartesian grid at this resolution are too small to effectively seed the instability. We perturbed the velocity on the grid with an $l = 8$ order Legendre polynomial with an amplitude 10% of the initial velocity. While this is probably unphysical, it represents a limiting case: The absence of Rayleigh-Taylor induced mixing with a perturbation this extreme implies its absence in the larger, lower resolution simulations is reasonable. The first $1 \times 10^3 \text{ s}$ of the simulation were run at this high resolution. By this point the Rayleigh-Taylor instabilities are clearly visible at the C-O/He boundary, but there is no hint of the development of this instability at the interface between the ^{56}Ni core and the overlying layers. Kifonidis et al. (2006) speculated that the reason they saw mixing at the Si/O boundary when earlier studies did not was the "ad hoc" initialization of these explosions with a piston or thermal bomb, insufficient resolution, or differences in structure between their progenitor models and those employed in previous studies. Insufficient resolution does not appear to be the case here, and our extreme perturbations imply that seeding perturbations through neutrino-driven convection by starting the simulation earlier would have little effect. We can only conclude that this is a valid result arising from the structure of our progenitor star, or a result of the piston explosion mechanism.

Because very little mixing occurs in the layers interior to the mass cut of these zero metallicity stars, their yields were very sensitive to the amount of fallback that occurs. Figure 23 shows this sensitivity. When the mass of infalling material was increased by 10% of the fiducial value taken from Zhang et al. (2008), almost none of the elements interior to the C-O shell escape. When the mass of infalling material was decreased by 10% of this fiducial value, more of the elements interior to oxygen escape and go on to enrich the surrounding gas. Figure 23 shows a comparison of the yields of our zero-metallicity stars with observations of the three most metal-poor stars yet found in the halo of the Milky Way. $[X/H]$ values for all elements were obtained by diluting the yields of our model stars with enough pristine gas to fit observations of $[C/H]$ and $[O/H]$ to individual halo stars. The dotted and dashed lines show the yields resulting from increasing or decreasing the amount of fallback by 10% of its fiducial value, respectively. Model z15D is more sensitive than Model z25D to decreasing the mass cut. The model yields appear much closer to fitting the values of elements heavier than oxygen observed in the metal-poor halo stars.

The yields of our Pop III core collapse supernovae reproduce the extreme overabundance of $[C,O/Fe]$ to the point where Fe is underproduced even when compared to the already low observations of $[C,O/Fe]$ in HMP stars. Carbon is slightly underproduced and nitrogen is underproduced by 2-3 dex relative to oxygen, as is the iron peak. The iron peak elements are underproduced because they do not mix sufficiently with the lighter elements in the star and cannot escape falling back onto the remnant at the center. A reduction in the infall mass brings z15D closer to reproducing observations. Two dimensional versions of the one dimensional simulations presented in the higher energy explosions of Heger & Woosley (2008) and Nomoto et al. (2007) might eject

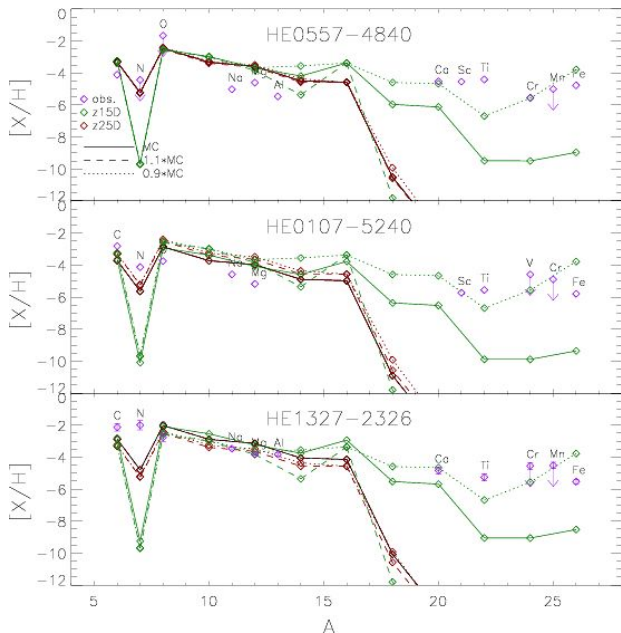


FIG. 23.— Model results matched to carbon and oxygen abundances found in individual HMP halo stars. Model z15D, with less fallback, expels some iron peak elements. Nitrogen is always under-produced, which is not a result of insufficient mixing during the supernova explosion but rather the presupernova evolution of these models. The solid line is the yield calculated using the remnant masses from Zhang et al. (2008). The dotted and dashed lines correspond to the amount of infall found in Zhang et al. (2008) decreased or increased by 10%, respectively. The sensitivity of the yields to fallback is especially apparent for Model z15D, the model with the least mixing.

more of the ^{56}Ni produced in the more energetic explosions. Rotating models (Hirschi et al. 2008) create more primary nitrogen, which can lead to an increase in the rate of CNO burning at the base of the hydrogen shell, causing some models die as larger red supergiants rather than a compact blue supergiants. In this case, Rayleigh-Taylor mixing would play out in a similar way to the solar models presented in this paper, and more iron would be ejected by these stars. Recent simulations (Scheck et al. 2004, 2006; Burrows et al. 2007a,b,c) point out that the supernova explosion mechanism is probably inherently multidimensional and asymmetric. Asymmetry in the explosion, whether in the form of a jet or a perturbation described by Legendre polynomials of order of $l = 1$ or $l = 2$, might also mix more of the nickel core out of the star, bringing the models closer to reproducing observations. Venn & Lambert (2008) have suggested that HMP stars may be “chemically peculiar” stars, in which low iron abundance is caused by separation of gas and dust beyond the stellar surface, followed by accretion of dust-depleted gas. If this is the case—and the authors note that a definitive answer requires additional information—the stars’ true metallicity is closer to $[X/H] \approx -2$ rather than -5 .

3.5. Visibility

The supernova light curve is affected by the amount of ^{56}Ni in the center of the star that falls back onto the black hole at the center of the explosion. The models for the first supernovae presented in this work are intrinsically dimmer than corresponding supernovae arising from stars of solar composition provided they ex-

plode with the same amount of energy. In our models of primordial composition supernovae, all or nearly all of the ^{56}Ni synthesized in the supernova falls back onto the remnant left behind at the center of the explosion. Energy from the radioactive decay of ^{56}Ni powers the tail of core-collapse supernova light curves. When the energy released in its radioactive decay to ^{56}Fe is no longer observable, the supernova light curves will lose their radioactive tails, making them briefer and dimmer than ordinary core-collapse supernova light curves.

4. CONCLUSIONS

The presupernova structure of a star is determined largely by its initial mass and by the initial composition of the gas from which it formed. The symmetry and energy of the explosion, along with the presupernova structure, influence where and to what extent Rayleigh-Taylor instabilities will grow, as well as how much mass will fall back onto the remnant at the center. The non-rotating zero metallicity models studied are far more compact than solar-composition models of the same mass, in part because CNO burning proceeds at higher temperatures and densities. CNO burning is responsible for energy production during the main sequence for all stars at the masses studied here, but in metal poor stars CNO burning proceeds at higher temperatures and densities. For zero-metallicity stars, the star must first contract to a temperature of 10^8 K, hot enough to initiate helium burning. This helium burning produces a small amount of carbon, which is enough to act as a catalyst to enable hot CNO burning to proceed. In addition, non-rotating stars with a metallicity Z below 10^{-3} will never reach the red giant branch, since they end helium burning with effective temperatures above 10^4 . Below this temperature, the opacity is large enough that the star will expand toward the red giant branch. The more compact structure of these stars causes their reverse shocks to propagate more quickly to the origin than those in solar stars. Larger remnants are left behind in the more compact stars because the rate at which mass accretes onto the stellar remnant is higher, as predicted by Chevalier (1989) and shown in the 1D simulations of Zhang et al. (2008).

The time scale over which the Rayleigh-Taylor instabilities can develop is also set by the reverse shock. For the case of the compact primordial composition progenitors modeled here, the Rayleigh-Taylor instabilities have little time to develop. This means that a smaller portion of the isotopic layers of the star will be mixed. The Rayleigh-Taylor instabilities do not have time to become fully nonlinear in our simulations, so the scale of the instability as well as the degree of mixing is set by the scale of the initial seed perturbations. In the case of the solar-composition progenitor models, the Rayleigh-Taylor instability became fully nonlinear and the size and shape of the initial perturbation was no longer apparent at late times. A smaller region of the primordial-composition stars is unstable, compared to solar-composition stars, which also contributes to the reduced mixing we see in our zero-metal models. The small amount of mixing experienced by zero-metallicity stars means that their yields are very sensitive to the amount of fallback, which may depend somewhat on the time the models were mapped from KEPLER to FLASH.

Unlike the recent simulations of Rayleigh-Taylor mixing in compact blue supergiants by Kifonidis et al. (2003, 2006), we do not see mixing at the silicon-oxygen shell interface. The absence of instability at that interface, as well as at the nickel-silicon shell interface in zD stars is robust. Mixing was not observed even after mapping the models to FLASH at earlier times, running the models at significantly higher resolution, and adding large perturbations of 10% to the velocity. Differences between the progenitor models used in Kifonidis et al. (2003, 2006) and our progenitor models, or structural differences arising from their early modeling and different explosion mechanism may be responsible. The degree of mixing we observe in our models is similar to that of earlier studies of compact blue supergiant progenitor models for SN 1987A. The degree of mixing and final velocities of isotopes we observe in our solar composition models is comparable to that found in Herant & Woosley (1994). Material from the silicon and nickel layers is mixed out into the outer layers of the solar metallicity stars, and these isotopes are mixed to velocities of $\sim 1 - 2 \times 10^3$ km s⁻¹, velocities comparable to those found in Herant & Woosley (1994).

The zero-metallicity models show a dramatic overproduction in carbon and oxygen relative to iron. This is the trend observed in the most metal-poor stars in the universe, but the degree of mixing in the present work is so small that not enough iron escapes to reproduce the already large [C+O/Fe] values observed in these stars. Decreasing the amount of fallback onto the remnant at the center through a more energetic explosion might succeed in driving more iron-peak isotopes out of the star, but would not result in a higher amount of nitrogen. Our models also cannot reproduce the [C/N] or [O/N] ratios observed in HMP stars. Zero-metallicity stars with significant rotation might produce both more primary nitrogen as well as more iron. Rotating models experience more shear mixing, which can drag primary carbon and oxygen from the ⁴He burning convective core to the ¹H

burning shell, where it becomes nitrogen, increasing the amount of burning in the ¹H shell and making that shell convective. The zero-metallicity stars may then die as a red, rather than blue, supergiant (Hirschi et al. 2008). If this is the case, then rotating zero-metallicity models might look very much like the solar-metallicity models presented in this paper, which would more closely reproduce abundances observed in HMP stars. A higher SN explosion energy might be another way to expel more iron from these stars.

Future work will include modeling primordial composition models with some degree of rotation, as recent work (Hirschi et al. 2008) indicates that they should have more primary nitrogen, as well as less compact structure and a larger ⁴He core. Modeling rotating stars may result in drastically different yields for our zero metallicity stars, allowing more iron to escape and increasing the [C/N] ratio closer to what is observed in HMP stars. We will explore higher explosion energies and asymmetric explosions and how they affect the amount of mixing.

The authors would like to thank Mike Zingale and Bruce Fryxell for assistance with the FLASH code, and Brian O'Shea and Gabriel Rockefeller for helpful comments on early drafts of this MS. The software used in this work was in part developed by the DOE-supported ASC / Alliance Center for Astrophysical Thermonuclear Flashes at the University of Chicago. This research has been supported by the NASA Theory Program NNG05GG08G and the DOE Program for Scientific Discovery through Advanced Computing (SciDAC; grants DOE-FC02-01ER41176 and DOE-FC02-06ER41438). At LANL, Heger and Joggerst performed this work under the auspices of the National Nuclear Security Administration of the U.S. Department of Energy at Los Alamos National Laboratory under Contract No. DE-AC52-06NA25396.

REFERENCES

- Aoki, W., Frebel, A., Christlieb, N., Norris, J. E., Beers, T. C., Minezaki, T., Barklem, P. S., Honda, S., Takada-Hidai, M., Asplund, M., Ryan, S. G., Tsangarides, S., Eriksson, K., Steinhauer, A., Deliyannis, C. P., Nomoto, K., Fujimoto, M. Y., Ando, H., Yoshii, Y., & Kajino, T. 2006, *ApJ*, 639, 897
- Arnett, D., Fryxell, B., & Mueller, E. 1989, *ApJ*, 341, L63
- Benz, W. & Thielemann, F.-K. 1990, *ApJ*, 348, L17
- Blair, W. P., Morse, J. A., Raymond, J. C., Kirshner, R. P., Hughes, J. P., Dopita, M. A., Sutherland, R. S., Long, K. S., & Winkler, P. F. 2000, *ApJ*, 537, 667
- Burrows, A., Dessart, L., & Livne, E. 2007a, in *American Institute of Physics Conference Series*, Vol. 937, American Institute of Physics Conference Series, ed. S. Immler & R. McCray, 370–380
- Burrows, A., Livne, E., Dessart, L., Ott, C. D., & Murphy, J. 2007b, *ApJ*, 655, 416
- , 2007c, *ApJ*, 655, 416
- Calder, A. C., Fryxell, B., Plewa, T., Rosner, R., Dursi, L. J., Weirs, V. G., Dupont, T., Robey, H. F., Kane, J. O., Remington, B. A., Drake, R. P., Dimonte, G., Zingale, M., Timmes, F. X., Olson, K., Ricker, P., MacNeice, P., & Tufo, H. M. 2002, *ApJS*, 143, 201
- Cayrel, R., Depagne, E., Spite, M., Hill, V., Spite, F., François, P., Plez, B., Beers, T., Primas, F., Andersen, J., Barbuy, B., Bonifacio, P., Molaro, P., & Nordström, B. 2004, *A&A*, 416, 1117
- Chevalier, R. A. 1976, *ApJ*, 207, 872
- , 1989, *ApJ*, 346, 847
- , 2005, *ApJ*, 619, 839
- Colella, P. & Woodward, P. R. 1984, *Journal of Computational Physics*, 54, 174
- Frebel, A., Aoki, W., Christlieb, N., Ando, H., Asplund, M., Barklem, P. S., Beers, T. C., Eriksson, K., Fechner, C., Fujimoto, M. Y., Honda, S., Kajino, T., Minezaki, T., Nomoto, K., Norris, J. E., Ryan, S. G., Takada-Hidai, M., Tsangarides, S., & Yoshii, Y. 2005, *Nature*, 434, 871
- Fryxell, B., Arnett, D., & Mueller, E. 1991, *ApJ*, 367, 619
- Fryxell, B., Olson, K., Ricker, P., Timmes, F. X., Zingale, M., Lamb, D. Q., MacNeice, P., Rosner, R., Truran, J. W., & Tufo, H. 2000, *ApJS*, 131, 273
- Hachisu, I., Matsuda, T., Nomoto, K., & Shigeyama, T. 1990, *ApJ*, 358, L57
- , 1992, *ApJ*, 390, 230
- Heger, A. & Woosley, S. E. 2008, *ArXiv e-prints*, 803
- Herant, M. & Benz, W. 1991, *ApJ*, 370, L81
- , 1992, *ApJ*, 387, 294
- Herant, M. & Woosley, S. E. 1994, *ApJ*, 425, 814
- Hirschi, R., Chiappini, C., Meynet, G., Maeder, A., & Ekstrom, S. 2008, *ArXiv e-prints*, 802
- Hughes, J. P., Rakowski, C. E., Burrows, D. N., & Slane, P. O. 2000, *ApJ*, 528, L109
- Iwamoto, N., Umeda, H., Tominaga, N., Nomoto, K., & Maeda, K. 2005, *Science*, 309, 451

- Kifonidis, K., Plewa, T., Janka, H.-T., & Müller, E. 2003, *A&A*, 408, 621
- Kifonidis, K., Plewa, T., Scheck, L., Janka, H.-T., & Müller, E. 2006, *A&A*, 453, 661
- Kurganov, A. & Tadmor, E. 2000, *Journal of Computational Physics*, 160, 241
- Mueller, E., Fryxell, B., & Arnett, D. 1991, *A&A*, 251, 505
- Nomoto, K., Tominaga, N., Tanaka, M., Maeda, K., & Umeda, H. 2007, in *American Institute of Physics Conference Series*, Vol. 937, American Institute of Physics Conference Series, ed. S. Immler & R. McCray, 412–426
- Scheck, L., Kifonidis, K., Janka, H.-T., & Müller, E. 2006, *A&A*, 457, 963
- Scheck, L., Plewa, T., Janka, H.-T., Kifonidis, K., & Müller, E. 2004, *Physical Review Letters*, 92, 011103
- Shu, C.-W. & Osher, S. 1989, *Journal of Computational Physics*, 83, 32
- Tominaga, N., Umeda, H., & Nomoto, K. 2007, *ApJ*, 660, 516
- Utrobin, V. P. 2004, *Astronomy Letters*, 30, 293
- Venn, K. A. & Lambert, D. L. 2008, *ArXiv e-prints*, 801
- Weaver, T. A., Zimmerman, G. B., & Woosley, S. E. 1978, *ApJ*, 225, 1021
- Weirs, G., Dwarkadas, V., Plewa, T., Tomkins, C., & Marr-Lyon, M. 2005, *Ap&SS*, 298, 341
- Witteborn, F. C., Bregman, J. D., Wooden, D. H., Pinto, P. A., Rank, D. M., Woosley, S. E., & Cohen, M. 1989, *ApJ*, 338, L9
- Woosley, S. E. 1988, *ApJ*, 330, 218
- Woosley, S. E. & Heger, A. 2007, *Phys. Rep.*, 442, 269
- Woosley, S. E., Heger, A., & Weaver, T. A. 2002, *Reviews of Modern Physics*, 74, 1015
- Woosley, S. E. & Weaver, T. A. 1995, *ApJS*, 101, 181
- Zhang, W., Woosley, S. E., & Heger, A. 2008, *ApJ*, 679, 639